

RESEARCH ARTICLE | DECEMBER 05 2023

Quantum correlation functions through tensor network path integral

Special Collection: [2023 JCP Emerging Investigators Special Collection](#)

Amartya Bose  



J. Chem. Phys. 159, 214110 (2023)

<https://doi.org/10.1063/5.0174338>



View
Online



Export
Citation

Articles You May Be Interested In

A multisite decomposition of the tensor network path integrals

J. Chem. Phys. (January 2022)

QuantumDynamics.jl: A modular approach to simulations of dynamics of open quantum systems

J. Chem. Phys. (May 2023)

Adaptive kink filtration: Achieving asymptotic size-independence of path integral simulations utilizing the locality of interactions

J. Chem. Phys. (March 2025)



The Journal of Chemical Physics

Special Topics Open for Submissions

[Learn More](#)

Quantum correlation functions through tensor network path integral

Cite as: J. Chem. Phys. 159, 214110 (2023); doi: 10.1063/5.0174338

Submitted: 30 August 2023 • Accepted: 7 November 2023 •

Published Online: 5 December 2023



View Online



Export Citation



CrossMark

Amartya Bose^{a)} 

AFFILIATIONS

Department of Chemical Sciences, Tata Institute of Fundamental Research, Mumbai 400005, India

Note: This paper is part of the 2023 JCP Emerging Investigators Special Collection.

^{a)} Author to whom correspondence should be addressed: amartya.bose@tifr.res.in

ABSTRACT

Tensor networks have historically proven to be of great utility in providing compressed representations of wave functions that can be used for the calculation of eigenstates. Recently, it has been shown that a variety of these networks can be leveraged to make real time non-equilibrium simulations of dynamics involving the Feynman–Vernon influence functional more efficient. In this work, a tensor network is developed for non-perturbatively calculating the equilibrium correlation function for open quantum systems using the path integral methodology. These correlation functions are of fundamental importance in calculations of rates of reactions, simulations of response functions and susceptibilities, spectra of systems, etc. The influence of the solvent on the quantum system is incorporated through an influence functional, whose unconventional structure motivates the design of a new optimal matrix product-like operator that can be applied to the so-called path amplitude matrix product state. This complex-time tensor network path integral approach provides an exceptionally efficient representation of the path integral, enabling simulations for larger systems strongly interacting with baths and at lower temperatures out to longer time. The derivation, design, and implementation of this method are discussed along with a wide range of illustrations ranging from rate theory and symmetrized spin correlation functions to simulation of response of the Fenna–Matthews–Olson complex to light.

Published under an exclusive license by AIP Publishing. <https://doi.org/10.1063/5.0174338>

I. INTRODUCTION

Equilibrium correlation functions provide deep insight into various quantum processes. Under the approximation of linear response and fluctuation–dissipation theorem,^{1,2} the response of a system to external stimuli is encoded in various two-time equilibrium correlation functions and Green's functions in a stimulus-independent manner.^{3–5} As a result, all spectra, including infrared spectra, UV–visible absorption, emission spectra, and multidimensional spectra, can be computed as Fourier transforms of different correlation functions.^{4,6} Quantum rate theories have been formulated in terms of equilibrium correlation functions involving the reactive flux operator.^{1,7–9} Spin–spin correlation functions are often used to study properties of spin-chains.

However, simulating these correlation functions can be quite challenging and approximations are regularly invoked.^{10–17} The computational cost grows prohibitively with the number of degrees

of freedom. Classical trajectory-based approaches are often used to approximate thermal correlation functions. Notable amongst these approaches are the family of semiclassical methods,^{14,18–20} centroid molecular dynamics,^{21,22} and ring-polymer molecular dynamics.^{23,24} However, these methods are best applied to systems where the quantum effects are primarily limited to quantum dispersion and zero-point energy effects. When quantum tunneling becomes important, a system–solvent decomposition is often very useful in limiting the exponential scaling of the quantum mechanics (QM) to a low-dimensional subspace. For small system–solvent coupling, various perturbation theory-based methods are used.^{15–17,25} When the coupling is large, approximations such as non-interacting blip approximation^{10,26,27} (NIBA) are quite common. However, these approximations do not provide computationally feasible routes to systematic improvements of accuracy and are consequently limited to particular parameter regimes.

Path integral methods have been derived for open quantum systems that enable the evaluation of correlation functions particularly in the context of calculating reaction rates. These methods are numerically exact and not subject to *ad hoc* approximations. They broadly fall into two categories: (1) path integral Monte Carlo-based and analytical continuation-based methods^{28,29} and (2) quadrature-based methods.^{29–32} The quadrature-based methods are typically derived on top of the quasi-adiabatic propagator path integral (QuAPI) and do not suffer from the dynamical sign problem that plagues the Monte Carlo approaches. This has enabled application of the method to calculation of reaction rates.^{31,33–36} However, despite the benefits, owing to the increase in non-Markovian memory length and a corresponding exponential growth of computational complexity and memory requirements, QuAPI for correlation functions can only be applied to relatively small systems.

Various approaches have been employed to reduce the complexity of the real-time non-equilibrium QuAPI calculations. Of particular interest amongst those are the ones based on tensor networks. Tensor networks are compact factorizations of large tensors and have been applied in a variety of ways to compress and estimate eigenstates of Hamiltonians through the density matrix renormalization group (DMRG).^{37–39} They have also shown incredible versatility in applications of time propagation of wave functions^{40–42} Inspired by the enormous computational benefits of such approaches, a number of developments have demonstrated the utility of tensor networks in alleviating some of the complexity of a QuAPI calculation.^{43–47} In fact, the multi-site tensor network path integral⁴⁶ (MS-TNPI) method, in particular, attempts to answer the question of what happens if the framework of time-dependent DMRG were extended to handle non-Markovian dynamics as seen in the dynamics of systems interacting with a solvent. These and other developments^{48–50} have enabled recent simulations of larger systems, which are computationally very challenging,^{51–54} and even small systems with strongly coupled baths, which have long memory lengths.^{43,45,53,54}

A natural curiosity stems from all of the recent development: Can a similar approach using tensor network be utilized to help with calculations of correlation functions as well? Would the benefits of tensor network compression be magnified in these equilibrium calculations? This article seeks to answer both the previous questions in the affirmative. Here, the path integral formulation of the equilibrium correlation function of an open quantum system is expressed in terms of tensor networks resulting in an efficient computational method. We discuss how a naïve implementation of such an idea suffers from long-range entanglement in the path integral tensor network structures, which can lead to much greater computational complexity. A procedure has to be developed that incorporates the structure inherent in these correlation functions and is able to keep the long-ranged correlations to a minimum.

The standard quantum correlation function suffers from a version of the dynamical sign problem because the forward- and backward-time propagators are pure phases that potentially cancel each other. However, the same physical information is contained in a different “complex-time” correlation function, where this interference of phases is significantly muted. The computational benefits of the exponentially decaying imaginary parts are quite well-known and have been previously used in innovative manners in conjunction

with Monte Carlo to increase the time spans of simulation.^{55,56} For these reasons, the current work only considers these complex-time correlation functions. Owing to the damping of the phases in a complex-time propagator, the complex-time tensor network path integral method introduced here is expected to have an even greater impact than that of the real-time non-equilibrium methods that preceded it. The same framework can and will be used for studying both dynamical properties at finite temperatures, such as spectra and susceptibilities, and equal-time or purely thermodynamic properties.

This paper is organized as follows. Section II describes the design and implementation of the tensor network for the complex-time correlation functions. Detailed discussions of the correlations between the points along the complex time contour and their impact on the structure of the tensor network are provided. Numerical examples of the complex-time tensor network path integral (CT-TNPI) are given in Sec. III. Illustrations of the method are taken from rate theory, simulations of symmetrized spin correlation functions (SSCF) and susceptibilities, and calculation of response functions of the Fenna–Matthews–Olson (FMO) complex. Finally, some future directions are discussed along with concluding remarks in Sec. IV.

II. METHOD

The standard quantum correlation function, which forms the basis of several observables, between operators \hat{A} and \hat{B} , is defined as

$$C_{\hat{A}\hat{B}}(t) = \frac{1}{Z} \text{Tr} \left(\exp(-\beta\hat{H}) \hat{A}(0) \hat{B}(t) \right), \quad (1)$$

where $\beta = \frac{1}{k_B T}$ is the inverse temperature, $Z = \text{Tr}(\exp(-\beta\hat{H}))$ is the partition function, and $\hat{B}(t) = \exp(i\hat{H}t/\hbar) \hat{B} \exp(-i\hat{H}t/\hbar)$ is the Heisenberg operator propagated to time t . Simulating this correlation function numerically is often quite challenging owing to the unmitigated phases in the Heisenberg operator $\hat{B}(t)$. The interference of these phases leads to a so-called “dynamical sign problem” for Monte Carlo simulations.

To avoid the sign problem, computational focus has primarily been on a related “complex-time” correlation function defined by

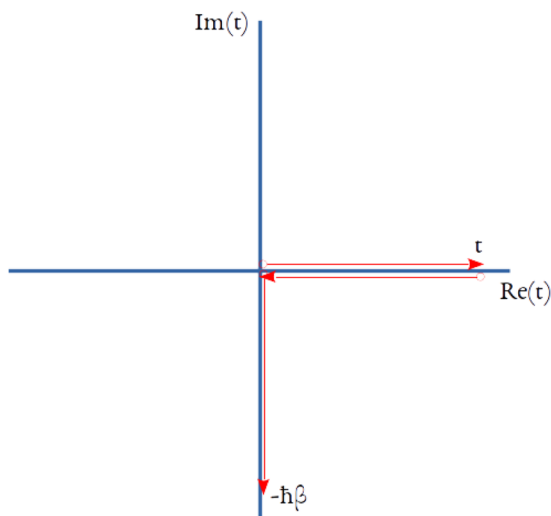
$$G_{\hat{A}\hat{B}}(t) = \frac{1}{Z} \text{Tr} \left(\hat{A}(0) \hat{B}(t_c) \right), \quad (2)$$

where $t_c = t - i\hbar\beta/2$ is the complex time. The phases in Eq. (2) are exponentially dampened by the decaying imaginary time terms, thereby reducing the dynamical sign problem. This complex-time correlation function contains the same dynamical information as the standard correlation function, Eq. (1), and is related to it in the Fourier domain by

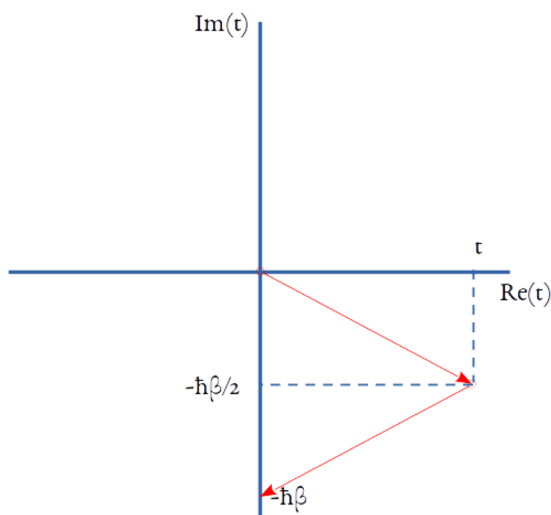
$$G_{\hat{A}\hat{B}}(\omega) = \exp\left(-\frac{\hbar\beta\omega}{2}\right) C_{\hat{A}\hat{B}}(\omega). \quad (3)$$

The time contours corresponding to Eqs. (1) and (2) are shown in Fig. 1.

The goal is to simulate correlation functions for systems interacting with N_{env} uncorrelated thermal environments. The operators, \hat{A} and \hat{B} , whose correlation function we are interested in, act on the



(a) Standard correlation function, Eq. 1



(b) Complex-time correlation function, Eq. 2

FIG. 1. Time contours for path integral representations of correlation functions.

system. The system along with the environments are described by the Hamiltonian,

$$\hat{H} = \hat{H}_0 + \sum_b^{N_{\text{env}}} \hat{H}_{\text{env}}^{(b)}, \quad (4)$$

$$\hat{H}_{\text{env}}^{(b)} = \sum_j \frac{P_{j,b}^2}{2m_{j,b}} + \frac{1}{2} m_{j,b} \omega_{j,b}^2 \left(x_{j,b} - \frac{c_{j,b} \hat{\sigma}^{(b)}}{m_{j,b} \omega_{j,b}^2} \right)^2. \quad (5)$$

The b th bath interacts with the system through the operator $\hat{\sigma}^{(b)}$. Here, we only consider the case where the different baths interact with the system through a commuting set of

operators. Hence, $[\hat{\sigma}^{(b_1)}, \hat{\sigma}^{(b_2)}] = 0$ for $b_1 \neq b_2$. Influence functional approaches for dealing with non-commuting operators have recently been derived.⁵⁷ The frequencies, $\omega_{j,b}$, and couplings, $c_{j,b}$, are characterized by the spectral density,

$$J_b(\omega) = \frac{\pi}{2} \sum_j \frac{c_{j,b}^2}{m_{j,b} \omega_{j,b}} \delta(\omega - \omega_{j,b}). \quad (6)$$

For molecular or atomistic environments, the corresponding harmonic bath can be obtained through simulations of the energy-gap correlation function.^{58,59}

To obtain the path integral representation for the thermal complex-time correlation function, Eq. (2), the correlation function is expressed as follows:

$$G_{\hat{A}\hat{B}}(t) = \frac{1}{Z} \text{Tr}_{\text{sys}}(\hat{A} \mathbb{O}_{\hat{B}(t_c)}), \quad (7)$$

where

$$\mathbb{O}_{\hat{B}(t_c)} = \text{Tr}_{\text{bath}}(\exp(i\hat{H}t_c/\hbar) \hat{B} \exp(-i\hat{H}t_c/\hbar)). \quad (8)$$

Once we are able to simulate $\mathbb{O}_{\hat{B}(t_c)}$ for arbitrary \hat{B} , Z can be obtained by setting \hat{B} to the identity operator in $Z = \text{Tr}_{\text{sys}}(\mathbb{O}_{\hat{B}(t_c)})$.

The final path integral expression for $\mathbb{O}_{\hat{B}(t_c)}$ for N time steps at a time point $t_c = N\Delta t_c$ is given as

$$\begin{aligned} \langle s_1 | \mathbb{O}_{\hat{B}(t_c)} | s_{2N+2} \rangle &= \sum_{s_2} \sum_{s_3} \cdots \sum_{s_{2N+1}} \langle s_1 | U^\dagger | s_2 \rangle \\ &\times \langle s_2 | U^\dagger | s_3 \rangle \cdots \langle s_N | U^\dagger | s_{N+1} \rangle \\ &\times \langle s_{N+1} | \hat{B} | s_{N+2} \rangle \\ &\times \langle s_{N+2} | U | s_{N+3} \rangle \cdots \langle s_{2N} | U | s_{2N+1} \rangle \\ &\times \langle s_{2N+1} | U | s_{2N+2} \rangle \times F[\{s_j\}] \end{aligned} \quad (9)$$

$$= \sum_{s_2} \sum_{s_3} \cdots \sum_{s_{2N+1}} P_{s_1, s_2, \dots, s_{2N+2}}^{(0)} F[\{s_j\}], \quad (10)$$

where $U = \exp(-i\hat{H}\Delta t_c/\hbar)$ and $U^\dagger = \exp(i\hat{H}\Delta t_c/\hbar)$ is the short time propagator corresponding to a time step of $\Delta t_c = (t - i\hbar\beta/2)/N$. The state $|s_j\rangle$ at the arbitrary j th time point is taken to be the simultaneous eigenkets of all the $\hat{\sigma}^{(b)}$ operators satisfying $\hat{\sigma}^{(b)} |s_j\rangle = s_j^{(b)} |s_j\rangle$. The product of the bare complex-time propagator elements (elements of U and U^\dagger) and the matrix element of \hat{B} can be grouped together to form the bare path amplitude tensor, $P_{s_1, s_2, \dots, s_{2N+2}}^{(0)}$. When the system operators corresponding to the bath interactions commute, the total influence functional, F , is a product of the influence functionals corresponding to the each of the uncorrelated baths,

$$F[\{s_j\}] = \prod_{b=1}^{N_{\text{env}}} F_b[\{s_j\}], \quad (11)$$

$$F^{(b)}[\{s_j\}] = \exp\left(-\frac{1}{\hbar} \sum_{k=1}^{2N+2} \sum_{k'=1}^k I_{kk'}^{(b)} s_k^{(b)} s_{k'}^{(b)}\right), \quad (12)$$

where $s_k^{(b)}$ is the eigenvalue of $\hat{\sigma}^{(b)}$ corresponding to the state of the system, s_k , at the k th time point. The diagonal terms of the influence functional matrix are

$$I_{kk}^{(b)} = \frac{2}{\pi} \int_0^\infty d\omega \frac{J(\omega)}{\omega^2 \sinh(\hbar\beta\omega/2)} \sin\left(\omega\left(\frac{t_{k+1}-t_k-i\hbar\beta}{2}\right)\right) \times \sin\left(\omega\left(\frac{t_{k+1}-t_k}{2}\right)\right), \quad (13)$$

and the off-diagonal terms are

$$I_{kk'}^{(b)} = \frac{4}{\pi} \int_0^\infty d\omega \frac{J(\omega)}{\omega^2 \sinh(\hbar\beta\omega/2)} \times \cos\left(\omega\left(\frac{t_{k+1}+t_k-t_{k'+1}-t_k-i\hbar\beta}{2}\right)\right) \times \sin\left(\omega\left(\frac{t_{k+1}-t_k}{2}\right)\right) \sin\left(\omega\left(\frac{t_{k'+1}-t_k}{2}\right)\right), \quad (14)$$

when $k \neq k'$.^{30,31} This symmetric $I^{(b)}$ -matrix is a discretization of the complex-time bath response function,

$$\alpha^{(b)}(\tau) = \sum_j \frac{c_{j,b}^2}{2m_{j,b}\omega_{j,b}} \frac{\cos\left(\omega_j\left(\tau+i\frac{\hbar\beta}{2}\right)\right)}{\sinh\left(\frac{\hbar\beta\omega_j}{2}\right)} \quad (15)$$

$$= \frac{1}{\pi} \int_0^\infty d\omega J_b(\omega) \frac{\cos\left(\omega\left(\tau+i\frac{\hbar\beta}{2}\right)\right)}{\sinh\left(\frac{\hbar\beta\omega}{2}\right)}, \quad (16)$$

Along the contour shown in Fig. 1(b). As observed by Shao and Makri,³³ the response function is maximum in the neighborhood of $t_c = 0$ and $t_c = -i\hbar\beta$. Unlike the real time bath correlation function,⁶⁰ though the complex-time α is finite everywhere, it does not decay with increasing $|t_c|$. However, note that α decays as $\text{Re}(t_c) \rightarrow \infty$ and as $\text{Im}(t_c) \rightarrow -i\hbar\beta/2$. The goal is to use this localization of non-Markovian interactions to generate compact tensor network representations of the path amplitude tensor.

Additionally, note that frameworks for simulation of the standard equilibrium correlation functions, Eq. (1), can also be used to calculate thermodynamic properties by simulating the so-called equal-time correlation functions. These are of the general form $C_{\hat{A}\hat{B}}(0) = \langle \hat{A}\hat{B} \rangle_\beta$. Similarly, the thermal expectation value of an operator can be written as $G_{\hat{A}\hat{B}}(0)$ if \hat{A} is the identity operator. While the bulk of this work deals with dynamical properties, we will give an example of the calculation of thermodynamic quantities.

To begin the process, observe that the bare path amplitude tensor only connects the nearest neighbors. Consequently, a matrix product representation of this tensor should be highly efficient. Consider the singular value factorizations of U , U^\dagger , and \hat{B} ,

$$U_{s_j, s_{j+1}}^\dagger = \sum_{\alpha_j} L_{s_j, \alpha_j}^{(\text{back})} R_{\alpha_j, s_{j+1}}^{(\text{back})}, \quad (17)$$

$$U_{s_j, s_{j+1}} = \sum_{\alpha_j} L_{s_j, \alpha_j}^{(\text{for})} R_{\alpha_j, s_{j+1}}^{(\text{for})}, \quad (18)$$

$$\hat{B}_{s_{N+1}, s_{N+2}} = \sum_{\alpha_{N+1}} B_{s_{N+1}, \alpha_{N+1}}^{(L)} B_{\alpha_{N+1}, s_{N+2}}^{(R)}. \quad (19)$$

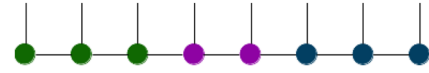


FIG. 2. Path amplitude matrix product state. Green sites correspond to those with U^\dagger , purple correspond to those with \hat{B} , and blue correspond to those with U .

In the above expressions, the singular value matrices have been absorbed into either the left or the right matrix. These factorized forms can be reassembled to create the matrix product state representation of the bare path amplitude tensor as follows:

$$P_{s_1, s_2, \dots, s_{2N+2}}^{(0)} = \sum_{\{\alpha_j\}} M_{s_1, \alpha_1}^{(1)} M_{\alpha_1, s_2, \alpha_2}^{(2)} \cdots M_{\alpha_{2N+1}, s_{2N+2}}^{(2N+2)}, \quad (20)$$

where

$$M_{s_1, \alpha_1}^{(1)} = L_{s_1, \alpha_1}^{(\text{back})}, \quad (21)$$

$$M_{\alpha_{j-1}, s_j, \alpha_j}^{(j)} = R_{\alpha_{j-1}, s_j}^{(\text{back})} L_{s_j, \alpha_j}^{(\text{back})}, \quad 2 \leq j \leq N, \quad (22)$$

$$M_{\alpha_N, s_{N+1}, \alpha_{N+1}}^{(N+1)} = R_{\alpha_N, s_{N+1}}^{(\text{back})} B_{s_{N+1}, \alpha_{N+1}}^{(L)}, \quad (23)$$

$$M_{\alpha_{N+1}, s_{N+2}, \alpha_{N+2}}^{(N+2)} = B_{\alpha_{N+1}, s_{N+2}}^{(R)} L_{s_{N+2}, \alpha_{N+2}}^{(\text{for})}, \quad (24)$$

$$M_{\alpha_{j-1}, s_j, \alpha_j}^{(j)} = R_{\alpha_{j-1}, s_j}^{(\text{for})} L_{s_j, \alpha_j}^{(\text{for})}, \quad N+3 \leq j \leq 2N+1, \quad (25)$$

$$M_{\alpha_{2N+1}, s_{2N+2}}^{(2N+2)} = R_{\alpha_{2N+1}, s_{2N+2}}^{(\text{for})}. \quad (26)$$

Here, α_j for $1 \leq j \leq 2N+1$ are the bond indices and their corresponding dimensions are the so-called “bond dimensions.” Because of the nearest neighbor nature of the terms in the bare path amplitude tensor in Eq. (9), the maximum of the bond dimensions will be equal to the dimensionality of the system. The \hat{B} operator has already been included in the bare path amplitude matrix product state (MPS) at sites $N+1$ and $N+2$. The path amplitude MPS is schematically shown in Fig. 2.

Now, the complex time influence functional needs to be incorporated. In order to accomplish this, we refactorize the total influence functional, Eq. (11), as a constrained product of terms representing interactions of one specific site, say, k , with all other sites,

$$F_k[\{s_j\}] = \exp\left(-\frac{1}{\hbar} \sum_{k'=1}^{2N+2} \sum_{b=1}^{N_{\text{env}}} I_{kk'}^{(b)} s_k^{(b)} s_{k'}^{(b)}\right). \quad (27)$$

In a direct implementation, there will be a double counting of every interaction in the product of terms such as Eq. (27). This double counting of interactions is avoided by tracing over the k th site immediately after applying F_k . The “constrain” is that the sum over k' in Eq. (27) will happen over the existing sites only. As a consequence, now when we move to, say, site $k+1$, F_{k+1} will not include the interaction between k and $k+1$ because that has already been

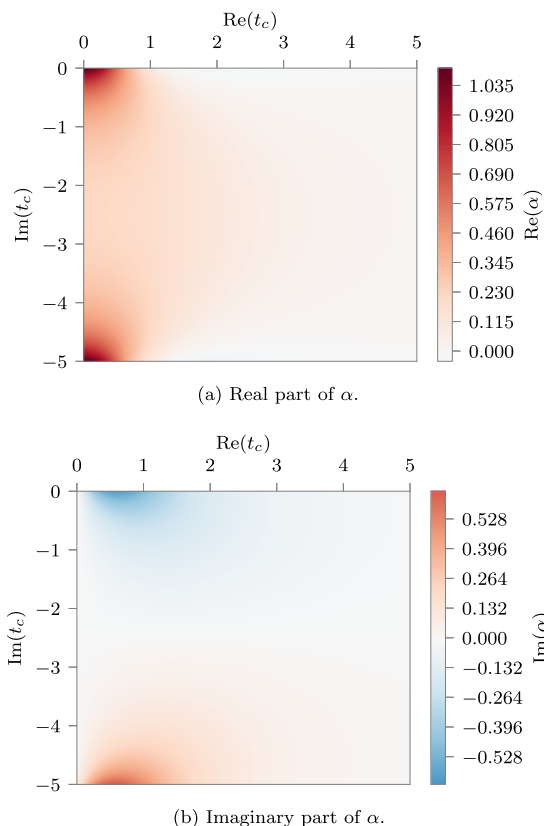


FIG. 3. Bath response function α as a function of complex time for an Ohmic spectral density with $\xi = 2$ and $\omega_c = 1$ at an inverse temperature of $\beta = 5$.

incorporated in the previous step. The procedure will be continued for the next chosen site. To be able to do this, there are two necessary problems that we have to solve: (1) we need to be able to provide a matrix product representation for the interaction of all sites with the k th site and (2) we need to come up with an ordering of the sites that minimizes the computational and storage requirements. In this, sites 1 and $2N + 2$ will not be traced over as they are required for the matrix representation of $\mathbb{O}_{\hat{B}(t_c)}$ and subsequent multiplication with \hat{A} .

Let us start with the second problem: assuming that we can represent the influence functional operator of all the interactions with site j , how do we order the application of these operators for maximal efficiency? Are there orderings that are better than others? As discussed, Fig. 3 demonstrates a decay of correlation as $\text{Re}(t_c)$ increases and $\text{Im}(t_c) \rightarrow -i\hbar\beta/2$. Hence, if we started applying the operator from site 2 and tracing it out, the correlations would initially decrease till $\text{Im}(t_c) = -i\hbar\beta/2$ but then increase till the end of the contour where $\text{Im}(t_c) = -i\hbar\beta$. These highly non-local interactions, which do not decay monotonically with distance along the complex time contour, would make the bond dimensions of the MPS grow very quickly on application of the influence functional matrix product operator (MPO). However, we can try to apply the influence functional operators in pairs from the middle outwards. This has the

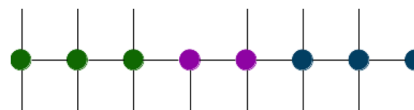


FIG. 4. Schematic of the first influence functional operator applied to the path amplitude MPS. The colors are only for helping synchronize this schematic with Fig. 2. Note that the site for which all interactions are included does not have an upper edge, indicating an automatic trace over the coordinate.

advantage of making the non-local interactions “look” short-ranged and, consequently, prevents the spurious growth of bond dimension in any other ordering. In fact, given the structure of α , going from $t_c = -i\hbar\beta/2$ outward toward $t_c = 0$ and $t_c = -i\hbar\beta$ is computationally the most optimal order of incorporation of the influence functional.

We will think in terms of multiple steps of incorporation of the influence functional, with each step consisting of incorporation of the non-Markovian interactions involving the middle two points. Hence, the first operator applied would take care of all non-Markovian interactions with site $N + 1$ and tracing over it. A schematic of this is shown in Fig. 4. This is not a typical matrix product operator (MPO). A key difference is that MPOs have the same number of downward and upward site indices. Here, the site whose interactions are being taken into account does not have an upward index. Consequently, the output MPS after application of the influence functional operator has one site less.

After application of the first influence functional operator, site number $N + 1$ ceases to exist. [To simplify our nomenclature, we will keep using the original numbering. Hence, though site $N + 2$, which has the information from the \hat{B} operator, is now the $(N + 1)$ th site, we will still refer to it as site $N + 2$. There is no site $N + 1$ now.] Then, the influence functional corresponding to site number $N + 2$ will be applied, with that site being traced over. (The influence functional corresponding to the $N + 2$ will not contain the interactions between the $N + 2$ th site and the $N + 1$ th site because this has been incorporated already before tracing over the latter. In this fashion, every subsequent influence functional will only consist of interactions between the sites that still exist.) This completes the first step of incorporation of the non-Markovian influence functional. Sites N and $N + 3$ would be incorporated in the second step, $N - 1$ and $N + 4$ in the third, so on and so forth till site 2 and $2N + 1$ are incorporated. The first couple of steps of the influence functional application are schematically shown in Fig. 5.

Having analyzed the structure of the non-Markovian memory and the order of application of the operators, we now derive the matrix-product representation for the complex-time influence functional connecting all the sites to a particular site k (for $2 \leq k \leq 2N + 1$). During the steps of application of the influence functional operators, we trace out sites from the middle of the contour. Let $l < k$ be the last remaining site to the left of the site k and $r > k$ be the first site immediately to the right of site k . At this stage of application, all the sites to the left of l ($j \leq l$) and right of r ($j \geq r$) must exist,

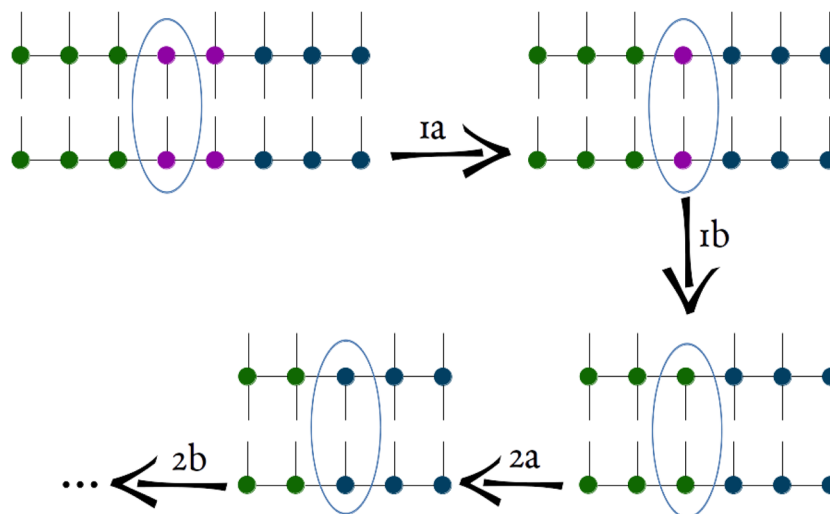


FIG. 5. First few steps of application of the influence functional operators. On application of the influence functional operator to the MPS, there is always one site with no dangling edges (no site index). This internal site is absorbed into the site that is left to it.

$$\begin{aligned}
 F_k[\{s_j\}] &= \sum_{\{\beta_j\}} \mathcal{F}_{s_1, s'_1, \beta_1}^{(1)} \mathcal{F}_{\beta_1, s_2, s'_2, \beta_2}^{(2)} \cdots \\
 &\times \mathcal{F}_{\beta_{l-1}, s_l, s'_l, \beta_l}^{(l)} \mathcal{F}_{\beta_l, s_k, \beta_{r-1}}^{(k)} \mathcal{F}_{\beta_{r-1}, s_r, s'_r, \beta_r}^{(r)} \\
 &\times \cdots \mathcal{F}_{\beta_{2N+1}, s_{2N+1}, s'_{2N+1}, \beta_{2N+1}}^{(2N+1)} \mathcal{F}_{\beta_{2N+1}, s_{2N+2}, s'_{2N+2}}^{(2N+2)}. \quad (28)
 \end{aligned}$$

Note that the tensor with index k has only one unprimed site index. This is the feature that enables the automatic tracing over the k th site and is shown in Fig. 4. The exact forms of the constituent tensors, \mathcal{F} , are listed in the Appendix A.

Now, we can define the complete algorithm for simulating the correlation function at a time point $N\Delta t$ as follows:

- Obtain the bare path amplitude MPS corresponding to $\mathbb{O}_{B(t_c)}$ with $2N + 2$ sites.
- Apply the influence functional operator corresponding to F_{N+1} , which encodes all the interactions with the $(N + 1)$ th time point along the complex time contour.
- Apply F_{N+2} . This completes the first step of the application of the influence functional, and now the path amplitude MPS has $2N$ sites. (We are still following our convention of retaining the time labels of the points.)
- Apply F_N and F_{N+3} . Path amplitude MPS now has $2N - 2$ sites.
- Repeat till path amplitude MPS has just two sites.
- Contract this two-site MPS into a matrix and apply the influence functional between sites 1 and $2N + 2$.
- Multiply by \hat{A} and trace to get the correlation function.

The computational complexity of any MPS-based method is determined by the maximum bond dimension of the MPS.^{38,41} Although the current CT-TNPI algorithm is not based on conventional MPO-MPS applications, the same arguments and ideas go

through. For every final time point, we have multiple influence functional operators acting on the path amplitude MPS in sequence, leading to a possible increase in the maximum bond dimension. We define $\bar{\beta}(t)$ as the average of the maximum bond dimensions encountered over the multiple MPO-MPS applications required for simulating the correlation function at a particular time, t . This measure governs the computational requirements of the method. A analysis of computational cost is given in Appendix B. Various common optimizations and singular value-based filtering schemes that are used in regular MPO-MPS application can be used here as well. These are typically governed by two convergence parameters: the cutoff threshold governing the truncated singular value decomposition (SVD) and the maximum bond dimension of the resulting MPS. Variational procedures may also be used for applying the influence functional operator to the path amplitude MPS.

III. RESULTS

As numerical illustrations of the method, we provide examples from rate theory, calculations of spin correlation functions and susceptibilities, and simulation of response functions of the Fenna–Mathews–Olson complex of photosynthesis. For the first two sets of examples, the system under study can be simply described by a symmetric spin-half particle or a two-level Hamiltonian,

$$\hat{H}_0 = -\hbar\Omega\sigma_x, \quad (29)$$

where σ_j for j in $\{x, y, z\}$ are the spin-1/2 Pauli matrices. There is one bath that couples to the system through the σ_z operator. In these model problems, the spectral density of the bath is taken to be of the general form

$$J(\omega) = \frac{\pi}{2} \hbar \xi \omega^s \omega_c^{1-s} \exp\left(-\frac{\omega}{\omega_c}\right), \quad (30)$$

where ω_c is the characteristic frequency of the bath and ξ is the dimensionless Kondo parameter encoding the strength of the system–environment coupling. The parameter s decides the nature of the spectral density, with $s = 1$ being the celebrated Ohmic form. The reorganization energy of the bath, given by

$$\lambda = \frac{2}{\pi} \int_{-\infty}^{\infty} \frac{J(\omega)}{\omega} d\omega, \quad (31)$$

evaluates to $\lambda = 2\hbar\xi\omega_c\Gamma(s)$. Thus, the reorganization energy of a sub-Ohmic spectral density ($s < 1$) is greater than that of an Ohmic bath with the same Kondo parameter.

A. Rate theory

For the first example, consider calculation of reaction rates. Many reactions happen at significantly slower time scales compared to the ro-translational motion of the reactants. In such cases, it becomes difficult to directly simulate the reaction, and one often resorts to calculations of reaction rates. While reaction rates can be calculated classically, such approaches miss out on quantum effects of nuclei and are generally unsuitable for purely non-adiabatic reactions, such as electron transport. It has been shown that the rate of a reaction is linked to the improper integral of the flux–flux correlation function over all time or the zero frequency component of the spectrum corresponding to the flux–flux correlation function,^{1,7–9}

$$k = \int_0^{\infty} C_{ff}(t) dt, \quad (32)$$

$$C_{ff}(t) = \frac{1}{Q} \text{Tr} \left(F \exp \left(i \frac{\hat{H}t_c^*}{\hbar} \right) F \exp \left(-i \frac{\hat{H}t_c}{\hbar} \right) \right), \quad (33)$$

where Q is the reactant partition function and $F = \frac{i}{\hbar} [\hat{H}, |R\rangle\langle R|]$ is the flux operator. An equivalent formulation can be built in terms of the long-time limit of the so-called “flux-side” correlation, which is the integral of the flux–flux correlation function,^{8,9}

$$k = \lim_{t \rightarrow \infty} C_{fs}(t), \quad (34)$$

$$C_{fs}(t) = \frac{1}{Q} \text{Tr} \left(F \exp \left(i \frac{\hat{H}t_c^*}{\hbar} \right) |R\rangle\langle R| \exp \left(-i \frac{\hat{H}t_c}{\hbar} \right) \right). \quad (35)$$

In condensed phase reactions, the infinite time limits in both the equations can be truncated to a plateau time t_{plateau} after which the flux-side correlation function becomes constant and the flux–flux correlation function becomes zero. One can think of the rate as half of the zero frequency component of a frequency-dependent rate function corresponding to the flux–flux autocorrelation function.²⁹ These quantum flux-based reaction rates have been simulated not just using equilibrium correlation functions, but approaches of using non-equilibrium³⁵ and near-equilibrium simulations³⁶ have also been shown to give the correct rates.

As a test of CT-TNPI, consider a two-state model for the symmetric proton transfer process where the tunneling splitting is much smaller than the vibronic frequencies. This separation of time scales, common in many reactions, is critical to the applicability of rate

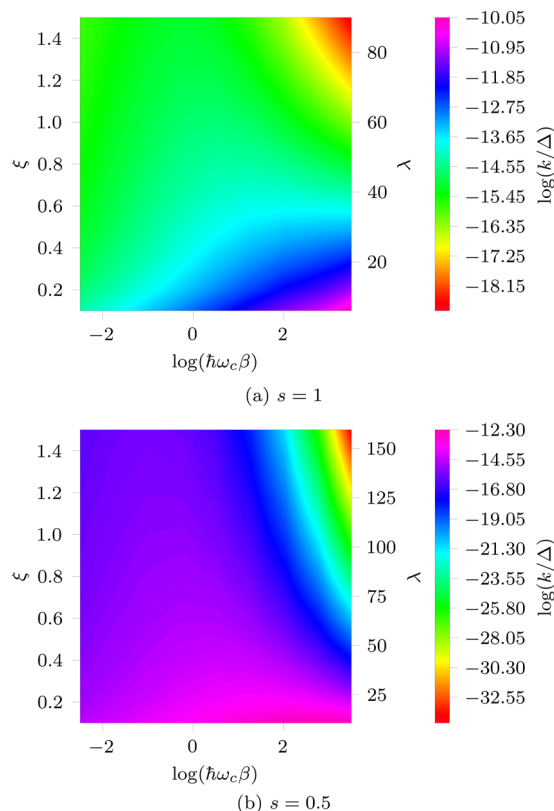


FIG. 6. Rates of reaction for a symmetric two-state system normalized to the tunneling splitting.

theory. Following Topaler and Makri,³¹ we choose a symmetric two-state system with a tunneling splitting of $\Delta = 2\hbar\Omega = 0.00105 \text{ cm}^{-1}$. The environment considered has the form given in Eq. (30) with a high cutoff frequency of $\omega_c = 500 \text{ cm}^{-1}$. We investigate the rates for the Ohmic case ($s = 1$), which is ubiquitous for condensed phase systems, and a sub-Ohmic case ($s = 0.5$). The rates for a range of temperatures and coupling strengths are shown in Fig. 6. The results for the Ohmic bath [Fig. 8(a)] have been previously discussed,³¹ and we obtain identical results with the CT-TNPI method, demonstrating the correctness of the approach. The data shown in Fig. 6 correspond to $N = 30$ and a cutoff threshold of 10^{-20} . These simulation parameters are significantly more accurate than what is necessary for convergence.

There are certain patterns that hold true for both the Ohmic and the sub-Ohmic spectral densities. The rates as a function of the Kondo parameter for a constant $\hbar\omega_c\beta$ (a vertical slice from Fig. 6) show a monotonic decrease, the rate of which is smaller at higher temperatures and larger at lower temperatures. On the other hand, if one takes a horizontal slice from these plots and studies the rate as a function of $\hbar\omega_c\beta$ at different values of the Kondo parameter, we notice variable behaviors. At low values of ξ , the rate increases with β , while at intermediate ξ , there is a non-monotonic behavior of the rate, which first increases and then decreases with increasing β . Note that the rate of reaction in presence of the sub-Ohmic bath is

always smaller than the ones in the presence of an Ohmic bath at the same Kondo parameters and temperatures. The ratio of the rate for the Ohmic bath and the sub-Ohmic bath becomes larger at colder temperatures and larger Kondo parameters going up to an order of 10^6 within the ranges of simulation.

To demonstrate the performance of the CT-TNPI method, we plot the flux-side correlation function and $\tilde{\beta}(t)$ for two particular Ohmic parameters in Fig. 7. These calculations were run with $N = 40$ and a cutoff threshold of 10^{-20} . Despite this, $\tilde{\beta}(t)$ is very small throughout the period of simulation, demonstrating the efficiency of the method. The magnitude of $\tilde{\beta}(t)$ is often dependent on the particular correlation function as we will numerically demonstrate in the next examples. According to Appendix B, $\mathcal{O}(\tilde{\beta}^3(t))$ provides an upper bound of the computational complexity. Hence, we note that the cost initially increases polynomially up to a critical time ($\omega_c t \approx 7.5$ for $\xi = 0.5$ and $\omega_c t \approx 10$ for $\xi = 0.1$), after which it drops down exponentially. This decrease in complexity is because of the efficiency SVD filtration in tackling the damped oscillations of the complex-time correlation function.

B. Symmetrized spin correlation functions

In addition to being useful for rate theory calculations, correlation functions are foundational in connecting to many observable quantities. One of the dynamical quantities of interest for the spin-boson model is the symmetrized spin correlation function (SSCF).^{10–13,15–17} Consider the SSCF for the σ_z operator defined as

$$S(t) = \frac{1}{2Z} \text{Tr} \left(\exp(-\beta \hat{H}) (\sigma_z(t) \sigma_z(0) + \sigma_z(0) \sigma_z(t)) \right), \quad (36)$$

which is related to the structure factor.²⁷ It captures the equilibrium fluctuations in the system. The spectrum of SSCF is related to the spectrum of the complex-time correlation function as

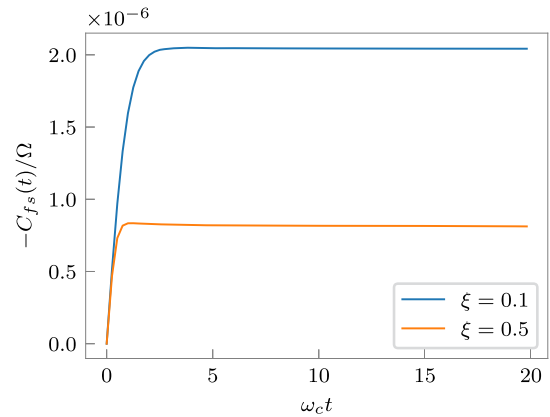
$$S(\omega) = \cosh \left(\frac{\hbar \omega \beta}{2} \right) G(\omega), \quad (37)$$

where $G(\omega) = \int_{-\infty}^{\infty} G(t) \exp(-i\omega t) dt$.

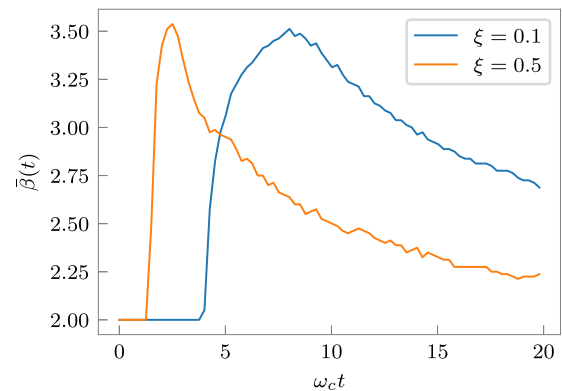
The SSCF spectrum can be studied using the celebrated non-interacting blip approximation (NIBA).¹⁰ Systematic perturbative expansions using a diagrammatic formulation for spin systems are difficult. This difficulty is relieved by mapping the spins to Majorana fermions.¹¹ The Majorana fermionic mapping has later led to developments of diagrammatic perturbation theories.^{12,13,15–17} However, while qualitatively consistent, it has been seen that there are subtle differences in the SSCF spectrum calculated by the Majorana fermionic approaches and the NIBA estimation.¹⁷ The CT-TNPI framework allows for numerically exact non-perturbative simulations of these quantities, and the converged results are consequently free from any uncontrolled approximations.

Additionally, suppose the system was additionally subject to a time-dependent external field, $F(t)$, through the interaction Hamiltonian

$$\hat{H}_{\text{int}}(t) = -\sigma_z F(t). \quad (38)$$



(a) Flux-side correlation function



(b) Bond dimension as a function of time

FIG. 7. Simulations for $\hbar\omega_c\beta = 0.2$. Both flux-side correlation function and the values of $\tilde{\beta}(t)$ shown for two different system–solvent couplings of $\xi = 0.1$ and $\xi = 0.5$.

Then, under linear response, the change in $\langle \sigma_z \rangle$ is given in terms of a dynamical susceptibility,^{1,2,5}

$$\delta \langle \sigma_z(t) \rangle = \int dt' \chi(t-t') F(t') \quad (39)$$

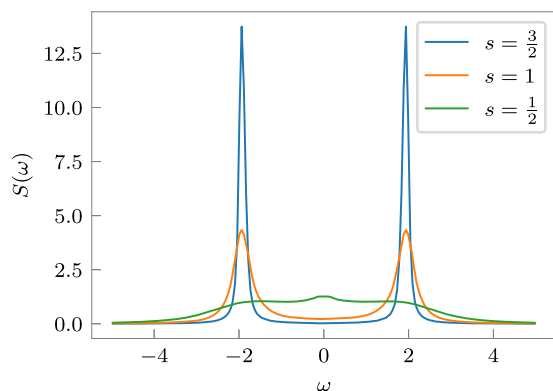
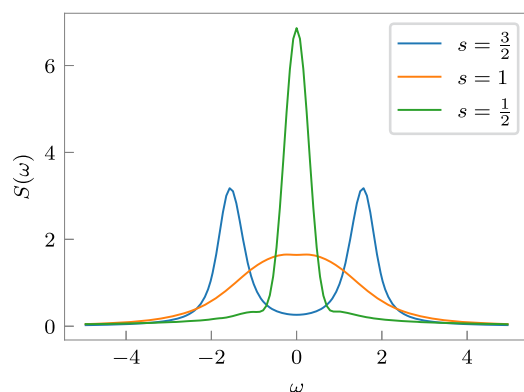
or

$$\delta \langle \sigma_z(\omega) \rangle = \chi(\omega) F(\omega), \quad (40)$$

where

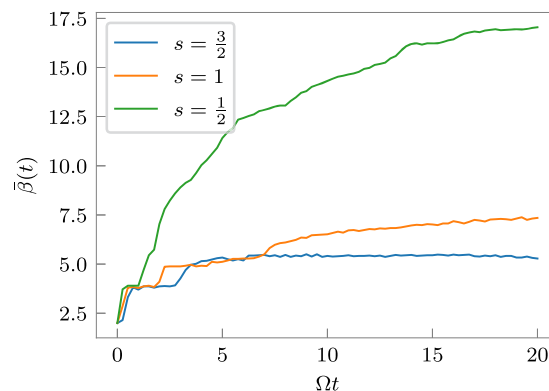
$$\chi(t) = \frac{i\Theta(t)}{Z} \text{Tr} \left(\exp(-\beta \hat{H}) (\sigma_z(t) \sigma_z(0) - \sigma_z(0) \sigma_z(t)) \right). \quad (41)$$

Consequently, the spectrum of total energy absorbed due to exposure to the external field $F(t)$ is related to $\text{Im}(\chi(\omega)) = \chi''(\omega)$ as $Q(\omega) = 2\omega |F(\omega)|^2 \chi''(\omega)$. This is equivalent to Fermi's Golden rule applied to the response of the system to the external field. Thus, $\chi''(\omega)$ captures the dissipation or absorption of energy by the system when perturbed by an external non-equilibrium field.

(a) Weakly coupled bath with $\xi = 0.03$.(b) Strongly coupled bath with $\xi = 0.18$.**FIG. 8.** Comparison of spectra corresponding to SSCF of the system coupled with Ohmic and non-Ohmic baths of different strengths.

Under the fluctuation–dissipation theorem,^{2,5} the Fourier transform of the imaginary part of the dynamical susceptibility, or the dissipation spectrum, is also related to the spectrum of SSCF, which is a measure of the equilibrium fluctuations of the system. This along with Kramer–Kronig’s relation allows us to estimate both the real $[\chi'(\omega)]$ and the imaginary $[\chi''(\omega)]$ parts of $\chi(\omega)$. Thus, it is possible to calculate the symmetrized correlation function as well as the dynamical susceptibility for open quantum systems directly with the CT-TNPI. However, since the imaginary part of susceptibility directly relates to energy absorption from an external field, we focus on that.

Consider a symmetric spin-boson Hamiltonian with a tunneling splitting $2\hbar\Omega = 2$ connected to a spectral density given by Eq. (30) with a high cutoff frequency of $\omega_c = 30\Omega$ held at a temperature of $\hbar\Omega\beta = 0.4$. We study SSCF for three different kinds of spectral densities defined by the value of s : we look at the Ohmic spectral density ($s = 1$), a sub-Ohmic spectral density ($s = 0.5$), and a super-Ohmic spectral density ($s = 1.5$). The SSCF spectra, encoding the frequency distribution of the equilibrium fluctuations, are shown in Fig. 8 for two different Kondo parameters ξ . The

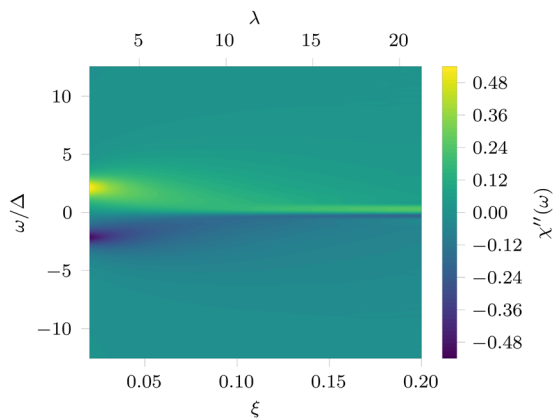
**FIG. 9.** Bond dimension for different baths with the Kondo parameter, $\xi = 0.03$.

correlation functions were converged for the time span under consideration with $N = 30$ steps and a cutoff threshold of 10^{-10} . As we go from sub-Ohmic to super-Ohmic, the oscillatory character of the dynamics, represented by the well-separated peaks of the SSCF spectrum, increases. The bond dimensions as characterized by $\beta(t)$ for all the three baths at a Kondo parameter of $\xi = 0.03$ are shown in Fig. 9. Note that in addition to the sub-Ohmic bath being the most efficient at dissipating the oscillatory dynamics, it also leads to the fastest growth of $\beta(t)$. In this case, the computational cost increases sharply initially but then slows down. Surprisingly, it becomes almost constant for the sub-Ohmic spectral density.

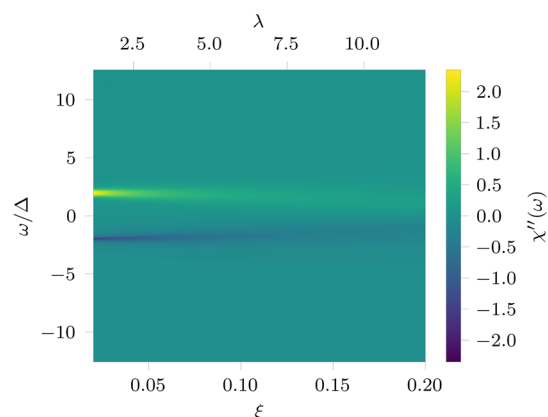
In Fig. 10, we track the imaginary part of the dynamical susceptibility spectrum at different system–solvent coupling strength for the Ohmic and sub-Ohmic ($s = 0.5$) cases. The energy absorption peak $[\chi''(\omega)]$ happens at $\pm\Omega$ for $\xi = 0$ and gets shifted to lower values on coupling to a bath with a greater Kondo parameter and consequently a larger reorganization energy. This shift happens significantly faster in the sub-Ohmic case than the Ohmic case, owing to the difference in reorganization energies in the two spectral densities at the same Kondo parameter. However, the reorganization energy is not the only factor that affects the susceptibility. The details of the spectral density matter as well. Note that the peaks for $\lambda \rightarrow 0$ are taller and sharper for the Ohmic spectral density. Similarly, $\chi''(\omega)$ is different between the Ohmic and sub-Ohmic spectral densities both at the same values of λ and ξ . Thus, the energy absorbed by the system from the external field at a particular frequency, ω , is highly dependent on the nature and strength of the system–solvent interactions. Because the path integral calculations are non-perturbative, unlike other approximations,^{17,61} the current approach gives the correct result at all parameters upon systematic convergence.

C. Fenna–Matthews–Olson complex

Now, let us explore the Fenna–Matthews–Olson (FMO) complex at an ambient temperature of $T = 300$ K. FMO is typically a trimer of octamers of chlorophyll molecules. Here, we consider only



(a) $\chi''(\omega)$ for sub-Ohmic spectral density ($s = 0.5$).



(b) $\chi''(\omega)$ for Ohmic spectral density ($s = 1$).

FIG. 10. Dynamical susceptibility for a spin-boson system for different bath spectral densities.

one octameric unit of the trimer as shown in Fig. 11. The system Hamiltonian is given as a Frenkel model,

$$\hat{H}_0 = \sum_{j=1}^8 \epsilon_j |j\rangle\langle j| + \sum_{j=1}^8 \sum_{l \neq j} h_{jl} (|j\rangle\langle l| + |l\rangle\langle j|), \quad (42)$$

where ϵ_j is the excitation energy of the j th chlorophyll molecule and h_{jl} is the electronic coupling between the excited state of the j th molecule and the ground state of the l th molecule. The basis $|j\rangle$ corresponds to the j th molecule being in the excited state and all other molecules in the ground state.

The vibronic couplings happen through localized vibrations and shifts between the ground and excited Born–Oppenheimer states. The vibrations of the j th molecule have the form

$$\hat{H}_{\text{vib}}^{(j)} = \sum_{i=1}^{N_{\text{osc}}} \frac{p_{i,j}^2}{2m_{i,j}} + \frac{1}{2} m_{i,j} \omega_{i,j}^2 \left(x_{i,j} - \frac{c_{i,j} |j\rangle\langle j|}{m_{i,j} \omega_{i,j}^2} \right)^2. \quad (43)$$

The system Hamiltonian and vibronic degrees of freedom are difficult to characterize. However, recent work⁶³ has provided accurate *ab initio* quantum-mechanics/molecular mechanics (QM/MM) level simulations of the spectral densities and the system Hamiltonians

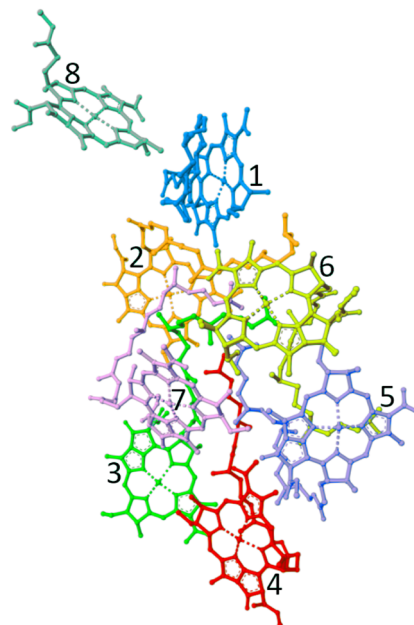


FIG. 11. Fenna–Matthews–Olson complex.

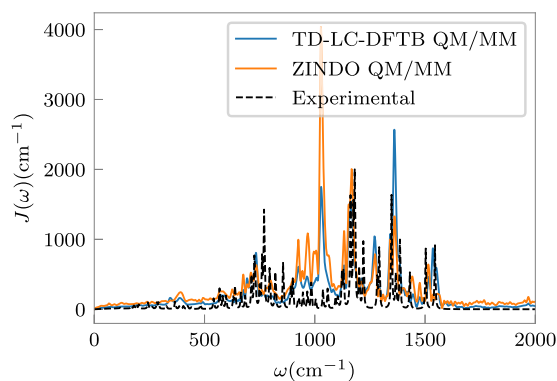


FIG. 12. Comparison of spectral densities for the FMO. The experimental spectral density⁶² is shown as a point of comparison with the simulated QM/MM spectral densities.⁶³

using the time-dependent long-range corrected density functional tight binding (TD-LC-DFTB) method and Zerner’s intermediate neglect of differential overlap (ZINDO) semi-empirical approach as the basis. The spectral density, averaged across all the eight monomers, is shown in Fig. 12. These descriptions have also been used to study the excitonic dynamics and pathways of transport.^{53,54}

The first question we ask is one of a static picture: If an initial excitation were to truly thermalize because of the vibronic coupling, what would the thermal density matrix of the electronic states be? This density matrix would have a single excitation. The (i, j) th element of the density matrix can be obtained by setting \hat{B} to identity and using $\hat{A} = |j\rangle\langle i|$ in the equation of $G_{\hat{A}\hat{B}}(t)$. The correlation function can be evaluated at any time as the real part of time cancels

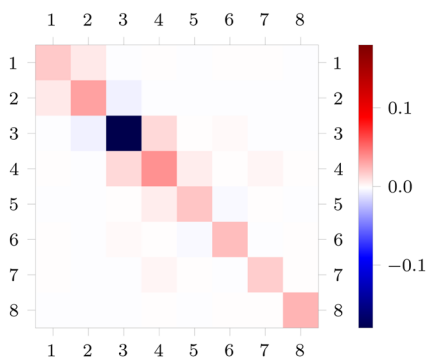


FIG. 13. Difference between the equilibrium density matrices for the TD-LC-DFTB parameterization and the ZINDO parameterization.

out. However, for convenience t was chosen to be 0. The simulation was run with $N = 20$ and a cutoff of 10^{-15} was used. The elements of the density matrix under different parameterization of the system Hamiltonian, \hat{H}_0 , and vibronic coupling are tabulated in Appendix C. Because of differences in the system Hamiltonian and vibronic couplings, these equilibrium density matrices are completely different. The difference is graphically shown in Fig. 13. Note that most of the differences are on or around the diagonal matrix elements. ZINDO significantly overestimates the equilibrium population on the third site and underestimates the populations on all the other sites. It is interesting that the difference also shows up in the purity of the thermal ensemble with the ZINDO equilibrium being significantly more pure [$\text{Tr}(\rho^2) = 0.938$] than the TD-LC-DFTB equilibrium density matrix [$\text{Tr}(\rho^2) = 0.63$]. The von Neumann entropies are also very different with ZINDO having very low entropy at 0.174 and TD-LC-DFTB being considerably more entangled at 0.91.

Finally, consider the FMO system being exposed to light. Generally, it is known that the absorption of the photon happens either on chlorophyll 1 or chlorophyll 6, and the sink where the excitation leads to further chemical reactions is molecule number 3. The Hamiltonian describing the interaction of the system with light under the dipolar approximation is

$$V(t) = -E(t)\hat{\mu}_j, \quad (44)$$

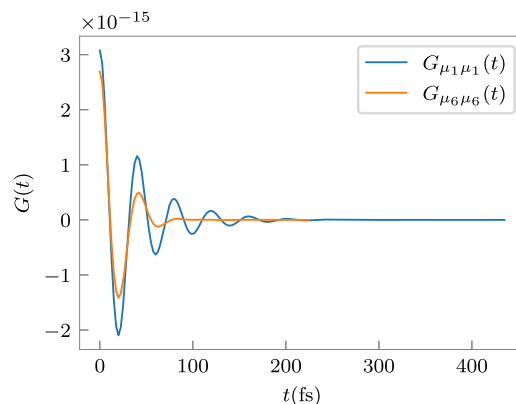
where $E(t)$ is the external electric field of the light and $\hat{\mu}_j = |j\rangle\langle 0| + |0\rangle\langle j|$ is the transition dipole operator for the j th molecule ($|0\rangle$ is the ground state, j is either 1 or 6). We want to understand how the expectation value of the dipole moment on the initially excited chlorophyll molecule changes as a result of this external perturbation. Under linear response,

$$\delta\langle\hat{\mu}_j(t)\rangle = \int dt' \chi(t-t')E(t'), \quad (45)$$

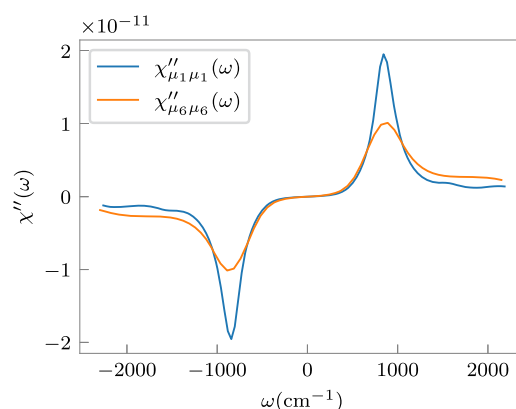
where

$$\chi(t) = i\Theta(t)\langle[\hat{\mu}_j(t), \hat{\mu}_j(0)]\rangle. \quad (46)$$

As discussed in the previous example, $\chi''(\omega)$ is related to the imaginary correlation function, $G_{\mu_j\mu_j}(\omega)$, as



(a) Complex-time correlation function corresponding to different states.



(b) Response function spectrum for different states.

FIG. 14. Correlation and response functions for the site-local dipole moment autocorrelation function.

$\chi''(\omega) = \sinh(\hbar\omega\beta/2)G_{\mu_j\mu_j}(\omega)$ and encodes the frequency dependent response of the j th chlorophyll to light incident on it. However, it is independent of the exact form of $E(t)$.

The complex-time correlation function, $G_{\mu_j\mu_j}(\omega)$, and the response function, $\chi''_{\mu_j\mu_j}(\omega)$, are shown in Fig. 14 for the TD-LC-DFTB parameters. Note that the auto-correlation function for $\hat{\mu}_6$ dies out much quicker than the one for $\hat{\mu}_1$. Consequently, it is possible to cause changes in $\hat{\mu}_6$ using a broader range of frequencies of light. In addition, because $\chi(t)$ is the Green's function, it encodes how the dipole moment on the j th site would change because of a delta function light pulse. The response to a particular pulse is obtained through convolution with the pulse shape, as shown in Eq. (45). The time-period of the decay gives the duration for which the oscillations in the molecular transition dipole moment persist on being exposed to a δ -function $E(t)$. There are two other small observations: first, the initial value of the correlation function is not 1 because the normalization is done using the canonical partition function, and second, we have not taken the magnitude of the molecular transition dipole moment into account, which would be a proportionality constant.

This dipole moment autocorrelation function can also yield information about the lifetimes of the molecular excitation. Toward that end, consider the lifetime of the molecular excitation on the j th chlorophyll. This can be measured using the decay time of the retarded Green's function $G_{\text{exc}}^R(t) = i\Theta(t)\left[\left[\hat{c}_j(t), \hat{c}_j^\dagger(0)\right]\right]$,⁶⁴ where \hat{c}_j annihilates an excitation on the j th molecule. This Green's function measures the amplitude of an excitation created on molecule j to remain on the same molecule after a time period t . The excitations on different molecules, being tightly-bound pairs of an electron and a hole, are bosonic in nature. Additionally, in our treatment, we are treating a maximum of one excitation per molecule, or $(\hat{c}_j^\dagger)^2 = 0$. This means that the molecular excitations are hard-core bosons. Now, we represent $\chi(t)$ in Eq. (46) in terms of these creation and annihilation operators using $\hat{\mu}_j = \hat{c}_j + \hat{c}_j^\dagger$,

$$\chi(t) = i\Theta(t)\left[\left[\hat{c}_j(t) + \hat{c}_j^\dagger(t), \hat{c}_j(0) + \hat{c}_j^\dagger(0)\right]\right] \quad (47)$$

$$= i\Theta(t)\left(\left[\left[\hat{c}_j(t), \hat{c}_j^\dagger(0)\right]\right] + \left[\left[\hat{c}_j^\dagger(t), \hat{c}_j(0)\right]\right]\right) \quad (48)$$

$$= 2i\text{Im}G_{\text{exc}}^R(t). \quad (49)$$

This damping is correlated with how long the excitation remains on the particular molecule or the “lifetime” of the molecular excitation. It can be shown that the $G_{\mu_j, \mu_j}(t)$ correlation can be related to the $\langle c_j(t)c_j^\dagger(0) \rangle$ correlation function where c_j annihilates an excitation on the j th molecule. This correlation function also measures the lifetime of a quasi-particle. Thus, we see that the lifetime of the molecular excitation on the first chlorophyll molecule lasts longer than the one on the sixth chlorophyll molecule.

IV. CONCLUSION

Equilibrium correlation functions form the basis for simulations of various experimentally relevant observables. When open quantum systems are involved, these correlation functions become difficult to simulate because of the exponential scaling of computational complexity with the number of degrees of freedom. Approximate approaches such as perturbation theory tend to fail either because of strong system–environment couplings or because they cannot be systematically converged. Path integrals and influence functional provide a lucrative way of rigorously incorporating non-perturbative influence of baths in these non-Markovian simulations. However, as the number of paths increase, both the computational and storage requirements tend to scale exponentially.

Tensor network is a commonly used framework of generating compact representations of tensors with large orders. Wide-ranging applications of tensor networks abound in physics^{37,40–42} and chemistry.^{65–67} In this article, we have presented a tensor network-based method for simulating thermal correlation functions for open quantum systems. A matrix product state is used to provide a compressed representation for the path amplitude tensor. We show that the non-Markovian correlations for the complex-time influence functional do not decay monotonically with the history. Hence, if the influence functional is naively represented as a matrix product operator, the path amplitude MPS

will not offer optimal compression. We use the structure of the bath response function to motivate an order of applying the influence functional that minimizes the growth of bond dimension and, consequently, is optimal from a computational perspective. Computationally, the tensor network backend opens up possibilities of future use of graphics processing units to further accelerate simulations. We have also derived the cost associated with the simulation.

Various simulations relating to rate theory, spin correlation functions, thermodynamics, and response functions have been used to illustrate the efficiency and broad applicability of the method. For the spin-boson model, we have calculated rates for parameters similar to the ones used for proton transfer reactions using the reactive flux theory and the spin–spin correlation functions, which encode how the spin reacts to external perturbation. We have applied the CT-TNPI method to simulate thermodynamics and dynamical properties of the Fenna–Matthews–Olson complex using rigorously defined vibronic couplings. Under linear response, the time-evolution of the change in the transition dipole moment of a particular chromophore under coupling to an external electromagnetic field is linked to a response function, which can be calculated at equilibrium. Using this, we have shown the correlation functions of the transition dipole moment corresponding to the sites numbered 1 and 6, which are most likely to get excited. We noted that the molecular excitation on the first chromophore has a larger lifetime than that on the sixth chromophore.

In the near future, we will focus on comparing vibrational dynamics of small molecules and rates of more complicated reactions in bulk and inside a cavity. Beyond these system specific studies, this work forms the first step in forming an infrastructure for multitime correlation functions that leverages tensor networks for greater efficiency. Such multitime correlation functions are related to various multidimensional spectra.⁴ Furthermore, the flexibility of the tensor network approaches allow us the ability to explore routes to equilibration starting from non-equilibrium initial conditions. Finally, the complex time tensor network path integral code developed in Julia⁶⁸ using the ITENSOR^{69,70} will be released soon as a part of the QuantumDynamics.jl⁷¹ library that was recently introduced as a platform for simulating dynamics in open quantum systems.

AUTHOR DECLARATIONS

Conflict of Interest

The author has no conflicts to disclose.

Author Contributions

Amartya Bose: Conceptualization (lead); Data curation (lead); Formal analysis (lead); Methodology (lead); Software (lead); Visualization (lead); Writing – original draft (lead).

DATA AVAILABILITY

The data that support the findings of this study are available from the corresponding author upon reasonable request.

APPENDIX A: INFLUENCE FUNCTIONAL OPERATORS

Below are the exact forms of the constituent tensors of the matrix product influence functional operator,

$$\mathcal{F}_{\beta_1 s_k, \beta_{r-1}}^{(k)} = \delta_{\beta_1 s_k} \delta_{\beta_{r-1}, s_k} \exp\left(-\frac{1}{\hbar} \sum_{b=1}^{N_{\text{env}}} I_{kk}^{(b)} s_k^{(b)} s_k^{(b)}\right), \quad (\text{A1})$$

$$\mathcal{F}_{\beta_{k'-1}, s_{k'}, \beta_{k'}}^{(k')} = \delta_{\beta_{k'-1}, \beta_{k'}} \exp\left(-\frac{1}{\hbar} \sum_{b=1}^{N_{\text{env}}} I_{kk'}^{(b)} \beta_{k'}^{(b)} s_{k'}^{(b)}\right), \quad (\text{A2})$$

$$\mathcal{F}_{s_1, \beta_1}^{(1)} = \exp\left(-\frac{1}{\hbar} \sum_{b=1}^{N_{\text{env}}} I_{1k}^{(b)} \beta_1^{(b)} s_1^{(b)}\right), \quad (\text{A3})$$

$$\mathcal{F}_{\beta_{2N+1}, s_{2N+2}}^{(2N+2)} = \exp\left(-\frac{1}{\hbar} \sum_{b=1}^{N_{\text{env}}} I_{k, 2N+2}^{(b)} \beta_{2N+1}^{(b)} s_{2N+2}^{(b)}\right). \quad (\text{A4})$$

On application of the influence functional operators, the number of sites on the path amplitude MPS decreases by one. The extra vertex that is left behind without a site index is absorbed conventionally in the vertex that is immediately to the right. With these definitions, we have a complete definition of the tensor networks required to simulate complex time correlation functions in a manner that optimally uses the structure of the complex-time bath response function.

APPENDIX B: COMPUTATIONAL COST

We want to estimate an approximate cost for simulating a correlation function of a system with d states out to time $N\Delta t$. CT-TNPI is essentially a method that uses repeated applications of matrix product operators to matrix product states. There are multiple methods of applying a matrix product operator to a matrix product state, each with its own cost.⁴¹ Here, for simplicity, we consider a direct MPO-MPS application and a subsequent truncation of the resultant MPS using singular value decomposition.

To simulate a correlation function at time $N\Delta t$ for a system with d states, we start with a bare path amplitude MPS with $2N+2$ sites and a constant bond dimension of d . All the influence functional MPOs have a bond dimension that corresponds to d as well. However, unlike other methods, CT-TNPI is further complicated by the fact that for every step, there are multiple $(2N)$ MPO-MPS applications with the length of the MPS shrinking by one after every application. Let β_L be the maximum bond dimension when the length of the MPS is L . Hence, $\beta(N\Delta t) = \frac{1}{2} \sum_{L=3}^{N+2} \beta_L$.

For a direct application of an MPO of length L with a bond dimension d to an MPS with bond dimension β_L , the final MPS that is truncated to have a bond dimension of β_{L-1} , is $\mathcal{O}(L\beta_L^3 d^4 + L\beta_L \beta_{L-1}^2 d^3)$. Note that the cost depends on the fourth power of the system dimensionality. Since d is a constant, it can be treated as a prefactor. Additionally, $\beta_L < \beta_{L-1}$ because MPO

application increases the entanglement between sites and correspondingly the maximum and average bond dimensions. Consequently, the second term in the cost for the L th step can be simplified to $\mathcal{O}(L\beta_{L-1}^3 d^4)$. Thus, the total cost of the L th step is $\mathcal{O}(Ld^4(\beta_L^3 + \beta_{L-1}^3))$.

Now, the total cost for simulating the correlation function out to $t = N\Delta t$ is

$$\kappa(N\Delta t) = \sum_{L=3}^{2N+2} \mathcal{O}(Ld^4(\beta_L^3 + \beta_{L-1}^3)) \quad (\text{B1})$$

$$= \sum_{L=3}^{2N+2} \mathcal{O}(Ld^4 \beta_L^3). \quad (\text{B2})$$

The rearrangement inequality states that if there are two sequences, x_i and y_i , ordered in the same sense,

$$\begin{aligned} x_1 y_N + \dots + x_N y_1 &\leq x_{\pi(1)} y_1 + \dots + x_{\pi(N)} y_N \\ &\leq x_1 y_1 + \dots + x_N y_N. \end{aligned} \quad (\text{B3})$$

This means that the “reverse” sum of two ordered sequences has the minimum value and the “direct” sum has the maximum value. All sums of random pairings have values in between these two extremes.

Now, for our case, the sequence β_L is ordered in a decreasing order with increasing L . Hence, the term $\sum_L L\beta_L^3$, which appears in Eq. (B2), is the reverse sum of the two sequences and has the minimum value. By averaging the values of all the P possible random sums, one can show that $\sum_L L\beta_L^3 < \bar{L} \sum_L \beta_L^3$, where $\bar{L} = \sum_L L/P$.

Because $\beta_L > 0$ for all L , $\bar{\beta}^3 > \frac{1}{8} \sum_L \beta_L^3$. (There are other cross-terms in $\bar{\beta}^3$.) Combining all these limits, the total cost can be re-expressed as

$$\kappa(t) = \mathcal{O}(d^4 \bar{\beta}^3(t)). \quad (\text{B4})$$

Thus, the cost of simulation of the correlation function at time t has an upper bound that goes as $d^4 \bar{\beta}^3(t)$. This is as compared to d^{2N+2} paths for a basic QuAPI simulation of the correlation function. (With filtration, the number of paths may be decreased even in the case of QuAPI.) The SVD filtration implicit in the MPS representation kills the exponential growth of complexity.

APPENDIX C: FMO EQUILIBRIUM DENSITY MATRICES

The equilibrium density matrices (rounded to 5 places of decimal) corresponding to FMO parameterized by different methods are

$$\rho_{\text{TD-LC-DFTB}}(300 \text{ K}) = \begin{pmatrix} 0.01993 & 0.00731 & -0.00261 & 0.00011 & -0.00032 & 0.00052 & 0.00017 & -0.00001 \\ 0.00731 & 0.03512 & -0.01087 & -0.00104 & -0.00012 & -0.00058 & -0.00013 & -0.00004 \\ -0.00261 & -0.01087 & 0.78816 & 0.02648 & 0.00211 & 0.00328 & -0.00298 & -0.00077 \\ 0.00011 & -0.00104 & 0.02648 & 0.04031 & 0.00621 & 0.00067 & 0.00314 & 0.00009 \\ -0.00032 & -0.00012 & 0.00212 & 0.00621 & 0.02243 & -0.00262 & 0.00031 & -0.00037 \\ 0.00052 & -0.00058 & 0.00328 & 0.00067 & -0.00262 & 0.0251 & -0.00096 & 0.00022 \\ 0.00017 & -0.00013 & -0.00298 & 0.00314 & 0.00031 & -0.00096 & 0.01915 & 0.00044 \\ -0.00001 & -0.00004 & -0.00077 & 0.00009 & -0.00037 & 0.00022 & 0.00044 & 0.0498 \end{pmatrix}, \quad (\text{C1})$$

$$\rho_{\text{ZINDO}}(300 \text{ K}) = \begin{pmatrix} 0.00067 & 0.00026 & -0.00123 & -0.00001 & -0.00001 & 0.00002 & 0.00001 & -0.0 \\ 0.00026 & 0.00171 & -0.00552 & -0.00011 & -0.00001 & -0.00004 & 0.00001 & -0.0 \\ -0.00123 & -0.00553 & 0.96801 & 0.01347 & 0.00072 & 0.0018 & -0.00203 & -0.00045 \\ -0.00001 & -0.00011 & 0.01347 & 0.00148 & 0.00025 & 0.00006 & 0.00009 & 0.00001 \\ -0.00001 & -0.00001 & 0.00072 & 0.00025 & 0.00141 & -0.00016 & 0.00001 & -0.00006 \\ 0.00002 & -0.00004 & 0.0018 & 0.00006 & -0.00016 & 0.00227 & -0.00006 & 0.00004 \\ 0.00001 & 0.00001 & -0.00203 & 0.00009 & 0.00001 & -0.00006 & 0.00121 & 0.00008 \\ -0.0 & -0.0 & -0.00045 & 0.00001 & -0.00006 & 0.00004 & 0.00008 & 0.02324 \end{pmatrix}. \quad (\text{C2})$$

REFERENCES

- ¹R. Kubo, "Statistical-mechanical theory of irreversible processes. I. General theory and simple applications to magnetic and conduction problems," *J. Phys. Soc. Jpn.* **12**, 570–586 (1957).
- ²R. Kubo, "The fluctuation-dissipation theorem," *Rep. Prog. Phys.* **29**, 255 (1966).
- ³D. Chandler, *Introduction to Modern Statistical Mechanics* (Oxford University Press, New York; Oxford, 1987).
- ⁴S. Mukamel, *Principles of Nonlinear Optical Spectroscopy, Oxford Series in Optical and Imaging Sciences Vol. 6* (Oxford University Press, New York, 1995).
- ⁵M. E. Tuckerman, *Statistical Mechanics: Theory and Molecular Simulation* (Oxford University Press, Oxford; New York, 2010).
- ⁶S. C. Althorpe, "Path-integral approximations to quantum dynamics," *Eur. Phys. J. B* **94**, 155 (2021).
- ⁷T. Yamamoto, "Quantum statistical mechanical theory of the rate of exchange chemical reactions in the gas phase," *J. Chem. Phys.* **33**, 281–289 (1960).
- ⁸W. H. Miller, "Quantum mechanical transition state theory and a new semiclassical model for reaction rate constants," *J. Chem. Phys.* **61**, 1823–1834 (1974).
- ⁹W. H. Miller, S. D. Schwartz, and J. W. Tromp, "Quantum mechanical rate constants for bimolecular reactions," *J. Chem. Phys.* **79**, 4889–4898 (1983).
- ¹⁰A. J. Leggett, S. Chakravarty, A. T. Dorsey, M. P. A. Fisher, A. Garg, and W. Zwerger, "Dynamics of the dissipative two-state system," *Rev. Mod. Phys.* **59**, 1–85 (1987).
- ¹¹A. M. Tsvelik, "New fermionic description of quantum spin liquid state," *Phys. Rev. Lett.* **69**, 2142–2144 (1992).
- ¹²W. Mao, P. Coleman, C. Hooley, and D. Langreth, "Spin dynamics from Majorana fermions," *Phys. Rev. Lett.* **91**, 207203 (2003).
- ¹³A. Shnirman and Y. Makhlin, "Spin-spin correlators in the Majorana representation," *Phys. Rev. Lett.* **91**, 207204 (2003).
- ¹⁴J. Liu and W. H. Miller, "Real time correlation function in a single phase space integral beyond the linearized semiclassical initial value representation," *J. Chem. Phys.* **126**, 234110 (2007).
- ¹⁵S. Florens, A. Freyn, D. Venturelli, and R. Narayanan, "Dissipative spin dynamics near a quantum critical point: Numerical renormalization group and Majorana diagrammatics," *Phys. Rev. B* **84**, 155110 (2011).
- ¹⁶P. Schad, "On the Majorana representation for spin 1/2," Ph.D. thesis, Karlsruhe Institut für Technologie, 2016.
- ¹⁷J. Liu, H. Xu, and C.-Q. Wu, "Green's functions for spin boson systems: Beyond conventional perturbation theories," *Chem. Phys.* **481**, 42–53 (2016).
- ¹⁸H. Wang, M. Thoss, and W. H. Miller, "Forward-backward initial value representation for the calculation of thermal rate constants for reactions in complex molecular systems," *J. Chem. Phys.* **112**, 47–55 (2000).
- ¹⁹H. Wang, M. Thoss, and W. H. Miller, "Systematic convergence in the dynamical hybrid approach for complex systems: A numerically exact methodology," *J. Chem. Phys.* **115**, 2979–2990 (2001).
- ²⁰W. H. Miller, "Including quantum effects in the dynamics of complex (i.e., large) molecular systems," *J. Chem. Phys.* **125**, 132305 (2006).
- ²¹J. Cao and G. A. Voth, "The formulation of quantum statistical mechanics based on the Feynman path centroid density. I. Equilibrium properties," *J. Chem. Phys.* **100**, 5093–5105 (1994).
- ²²J. Cao and G. A. Voth, "The formulation of quantum statistical mechanics based on the Feynman path centroid density. II. Dynamical properties," *J. Chem. Phys.* **100**, 5106–5117 (1994).
- ²³I. R. Craig and D. E. Manolopoulos, "Quantum statistics and classical mechanics: Real time correlation functions from ring polymer molecular dynamics," *J. Chem. Phys.* **121**, 3368–3373 (2004).

- ²⁴S. Habershon, D. E. Manolopoulos, T. E. Markland, and T. F. Miller, “Ring-polymer molecular dynamics: Quantum effects in chemical dynamics from classical trajectories in an extended phase space,” *Annu. Rev. Phys. Chem.* **64**, 387–413 (2013).
- ²⁵P. Schad, Yu. Makhlin, B. Narozhny, G. Schön, and A. Shnirman, “Majorana representation for dissipative spin systems,” *Ann. Phys.* **361**, 401–422 (2015).
- ²⁶H. Dekker, “Noninteracting-blip approximation for a two-level system coupled to a heat bath,” *Phys. Rev. A* **35**, 1436–1437 (1987).
- ²⁷U. Weiss, *Quantum Dissipative Systems*, 3rd ed. (World Scientific, 2012).
- ²⁸E. Rabani, G. Krilov, and B. J. Berne, “Quantum mechanical canonical rate theory: A new approach based on the reactive flux and numerical analytic continuation methods,” *J. Chem. Phys.* **112**, 2605–2614 (2000).
- ²⁹E. Sim, G. Krilov, and B. J. Berne, “Quantum rate constants from short-time dynamics: An analytic continuation approach,” *J. Phys. Chem. A* **105**, 2824–2833 (2001).
- ³⁰M. Topaler and N. Makri, “Quasi-adiabatic propagator path integral methods. Exact quantum rate constants for condensed phase reactions,” *Chem. Phys. Lett.* **210**, 285–293 (1993).
- ³¹M. Topaler and N. Makri, “Quantum rates for a double well coupled to a dissipative bath: Accurate path integral results and comparison with approximate theories,” *J. Chem. Phys.* **101**, 7500–7519 (1994).
- ³²M. Topaler and N. Makri, “Path integral calculation of quantum nonadiabatic rates in model condensed phase reactions,” *J. Phys. Chem.* **100**, 4430–4436 (1996).
- ³³J. Shao and N. Makri, “Iterative path integral calculation of quantum correlation functions for dissipative systems,” *Chem. Phys.* **268**, 1–10 (2001).
- ³⁴J. Shao and N. Makri, “Iterative path integral formulation of equilibrium correlation functions for quantum dissipative systems,” *J. Chem. Phys.* **116**, 507–514 (2002).
- ³⁵A. Bose and N. Makri, “Non-equilibrium reactive flux: A unified framework for slow and fast reaction kinetics,” *J. Chem. Phys.* **147**, 152723 (2017).
- ³⁶A. Bose and N. Makri, “Quasiclassical correlation functions from the Wigner density using the stability matrix,” *J. Chem. Inf. Model.* **59**, 2165–2174 (2019).
- ³⁷S. R. White, “Density matrix formulation for quantum renormalization groups,” *Phys. Rev. Lett.* **69**, 2863–2866 (1992).
- ³⁸U. Schollwöck, “The density-matrix renormalization group in the age of matrix product states,” *Ann. Phys.* **326**, 96–192 (2011).
- ³⁹U. Schollwöck, “The density-matrix renormalization group: A short introduction,” *Philos. Trans. R. Soc., A* **369**, 2643–2661 (2011).
- ⁴⁰S. R. White and A. E. Feiguin, “Real-time evolution using the density matrix renormalization group,” *Phys. Rev. Lett.* **93**, 076401 (2004).
- ⁴¹S. Paeckel, T. Köhler, A. Swoboda, S. R. Manmana, U. Schollwöck, and C. Hubig, “Time-evolution methods for matrix-product states,” *Ann. Phys.* **411**, 167998 (2019).
- ⁴²S. R. White, “Minimally entangled typical quantum states at finite temperature,” *Phys. Rev. Lett.* **102**, 190601 (2009).
- ⁴³A. Strathearn, P. Kirton, D. Kilda, J. Keeling, and B. W. Lovett, “Efficient non-Markovian quantum dynamics using time-evolving matrix product operators,” *Nat. Commun.* **9**, 3322 (2018).
- ⁴⁴M. R. Jørgensen and F. A. Pollock, “Exploiting the causal tensor network structure of quantum processes to efficiently simulate non-Markovian path integrals,” *Phys. Rev. Lett.* **123**, 240602 (2019).
- ⁴⁵A. Bose and P. L. Walters, “A tensor network representation of path integrals: Implementation and analysis,” [arXiv:2106.12523](https://arxiv.org/abs/2106.12523) (2021).
- ⁴⁶A. Bose and P. L. Walters, “A multisite decomposition of the tensor network path integrals,” *J. Chem. Phys.* **156**, 024101 (2022).
- ⁴⁷A. Bose, “Pairwise connected tensor network representation of path integrals,” *Phys. Rev. B* **105**, 024309 (2022).
- ⁴⁸J. Cerrillo and J. Cao, “Non-Markovian dynamical maps: Numerical processing of open quantum trajectories,” *Phys. Rev. Lett.* **112**, 110401 (2014).
- ⁴⁹N. Makri, “Modular path integral methodology for real-time quantum dynamics,” *J. Chem. Phys.* **149**, 214108 (2018).
- ⁵⁰N. Makri, “Small matrix path integral for system-bath dynamics,” *J. Chem. Theory Comput.* **16**, 4038–4049 (2020).
- ⁵¹S. Kundu and N. Makri, “Real-time path integral simulation of exciton-vibration dynamics in light-harvesting bacteriochlorophyll aggregates,” *J. Phys. Chem. Lett.* **11**, 8783–8789 (2020).
- ⁵²A. Bose and P. L. Walters, “Tensor network path integral study of dynamics in B850 LH2 ring with atomistically derived vibrations,” *J. Chem. Theory Comput.* **18**, 4095–4108 (2022).
- ⁵³A. Bose and P. L. Walters, “Impact of solvent on state-to-state population transport in multistate systems using coherences,” *J. Chem. Theory Comput.* **19**, 4828–4836 (2023).
- ⁵⁴A. Bose and P. L. Walters, “Impact of spatial inhomogeneity on excitation energy transport in the Fenna–Matthews–Olson complex,” *J. Phys. Chem. B* **127**, 7663–7673 (2023).
- ⁵⁵D. Thirumalai and B. J. Berne, “Time correlation functions in quantum systems,” *J. Chem. Phys.* **81**, 2512–2513 (1984).
- ⁵⁶B. J. Berne, “Path integral Monte Carlo methods: Static- and time-correlation functions,” *J. Stat. Phys.* **43**, 911–929 (1986).
- ⁵⁷T. Palm and P. Nalbach, “Quasi-adiabatic path integral approach for quantum systems under the influence of multiple non-commuting fluctuations,” *J. Chem. Phys.* **149**, 214103 (2018).
- ⁵⁸N. Makri, “The linear response approximation and its lowest order corrections: An influence functional approach,” *J. Phys. Chem. B* **103**, 2823–2829 (1999).
- ⁵⁹A. Bose, “Zero-cost corrections to influence functional coefficients from bath response functions,” *J. Chem. Phys.* **157**, 054107 (2022).
- ⁶⁰N. Makri and D. E. Makarov, “Tensor propagator for iterative quantum time evolution of reduced density matrices. I. Theory,” *J. Chem. Phys.* **102**, 4600–4610 (1995).
- ⁶¹D. Xu and J. Cao, “Non-canonical distribution and non-equilibrium transport beyond weak system-bath coupling regime: A polaron transformation approach,” *Front. Phys.* **11**, 110308 (2016).
- ⁶²M. Rätsep and A. Freiberg, “Electron-phonon and vibronic couplings in the FMO bacteriochlorophyll *a* antenna complex studied by difference fluorescence line narrowing,” *J. Lumin.* **127**, 251–259 (2007).
- ⁶³S. Maity, B. M. Bold, J. D. Prajapati, M. Sokolov, T. Kubař, M. Elstner, and U. Kleinekathöfer, “DFTB/MM molecular dynamics simulations of the FMO light-harvesting complex,” *J. Phys. Chem. Lett.* **11**, 8660–8667 (2020).
- ⁶⁴R. D. Mattuck, *A Guide to Feynman Diagrams in the Many-Body Problem*, 2nd ed. (Dover Publications, New York, 1992).
- ⁶⁵G. K.-L. Chan and S. Sharma, “The density matrix renormalization group in quantum chemistry,” *Annu. Rev. Phys. Chem.* **62**, 465–481 (2011).
- ⁶⁶J. Ren, Z. Shuai, and G. Kin-Lic Chan, “Time-dependent density matrix renormalization group algorithms for nearly exact absorption and fluorescence spectra of molecular aggregates at both zero and finite temperature,” *J. Chem. Theory Comput.* **14**, 5027–5039 (2018).
- ⁶⁷R. Olivares-Amaya, W. Hu, N. Nakatani, S. Sharma, J. Yang, and G. K.-L. Chan, “The *ab-initio* density matrix renormalization group in practice,” *J. Chem. Phys.* **142**, 034102 (2015).
- ⁶⁸J. Bezanson, A. Edelman, S. Karpinski, and V. B. Shah, “Julia: A fresh approach to numerical computing,” *SIAM Rev.* **59**, 65–98 (2017).
- ⁶⁹M. Fishman, S. White, and E. Stoudenmire, “The ITensor software library for tensor network calculations,” *SciPost Phys. Codebases* **4**, 1–53 (2022).
- ⁷⁰M. Fishman, S. White, and E. Stoudenmire, “Codebase release 0.3 for ITensor,” *SciPost Phys. Codebases* **4-r0.3** (2022).
- ⁷¹A. Bose, “QuantumDynamics.jl: A modular approach to simulations of dynamics of open quantum systems,” *J. Chem. Phys.* **158**, 204113 (2023).